catalysts

MDPI

Article

Graphyne Nanotubes as Promising Sodium-Ion Battery Anodes

Yuan Yuan [1,†], Xiaoxue Song [2,†], Jiapeng Ma [1], Yanqi Chen [1], Fangfang Wang [1], Baotao Kang [1,2,*] and Jin Yong Lee [2,*]

[1] School of Chemistry and Chemical Engineering, University of Jinan, Jinan 250022, China; chm_yuany@mail.ujn.edu.cn (Y.Y.); 202021100219@mail.ujn.edu.cn (J.M.); hauwkj@outlook.com (Y.C.); chm_wangff@ujn.edu.cn (F.W.)

[2] Department of Chemistry, Sungkyunkwan University, Suwon 16419, Korea; songxiaoxue@skku.edu

* Correspondence: chm_kangbt@ujn.edu.cn (B.K.); jinylee@skku.edu (J.Y.L.); Tel.: +86-531-8276-5961 (B.K.); +82-31-299-4560 (J.Y.L.)

† These authors contributed equally to this work.

Abstract: Sodium-ion batteries (SIBs) are promising candidates for the replacement of lithium-ion batteries (LIBs) because of sodium's abundant reserves and the lower cost of sodium compared to lithium. This is a topic of interest for developing novel anodes with high storage capacity. Owing to their low cost, high stability, and conductivity, carbon-based materials have been studied extensively. However, sp^2-C based carbon materials have low-rate capacities. Intensive density functional theory calculations have been implemented to explore the applicability of α, β, and γ graphyne nanotubes (αGyNTs, βGyNTs, and γGyNTs, respectively) as SIB anodes. Results suggest that (3, 0)-αGyNT, (2, 2)-βGyNT, and (4, 0)-γGyNT have, respectively, maximum Na storage capacities of 1535, 1302, and 1001 mAh/g, which exceeds the largest reported value of carbon materials (N-doped graphene foams with 852.6 mAh/g capacity). It was determined that αGyNTs have the largest storage capacity of the three types because they possess the largest specific surface area. Moreover, the larger pores of αGyNTs and βGyNTs allow easier diffusion and penetration of Na atoms compared to those of γGyNTs, which could result in better rate capacity.

Keywords: graphyne; secondary battery; DFT; curvature effect

Citation: Yuan, Y.; Song, X.; Ma, J.; Chen, Y.; Wang, F.; Kang, B.; Lee, J.Y. Graphyne Nanotubes as Promising Sodium-Ion Battery Anodes. *Catalysts* **2022**, *12*, 670. https://doi.org/10.3390/catal12060670

Academic Editor: Lihua Bi

Received: 11 May 2022
Accepted: 15 June 2022
Published: 19 June 2022

1. Introduction

The large-scale use of renewable energies would not only solve the urgent need to alleviate energy shortages, but also reduce the emissions of greenhouse gases in the push toward carbon neutrality [1]. To maximize the utilization of renewable energies, convenient and efficient storage equipment is essential [2]. Electrochemical batteries often play this important role due to their high stability and efficiency. Lithium-ion batteries (LIBs), first proposed by M.S. Whittingham in the 1970s [3], are a well-developed technology that has been applied widely in various fields [4,5]. Although LIBs can provide ultra-high specific capacity and energy density, lithium has limited abundance and is distributed non-uniformly within the earth's crust. In the future, the demand for green energy equipment will increase rapidly, leading to rising costs of LIBs [6]. Therefore, it is imperative to find alternatives to lithium.

When compared to the rare, light metal lithium, sodium is distributed widely on land and in the sea in the form of salt, and is of much lower cost than Li [7]. Though differences in radius and mass affect the capacity and transportation properties [8], sodium and lithium are both alkali metals, and are close in the periodic table of elements, resulting in similar properties. Thus, sodium has been regarded as the most promising alternative for replacing Li in new generations of secondary batteries, which has become a high priority in the past decade [9]. Currently, the materials that have been applied for SIB anodes include: sodium metal [10,11], carbon-based materials [12,13], alloys [14], organic electrodes [15],

and composites [16,17]. Although the specific capacity of sodium metal as SIB anodes can be comparable to that of LIBs [18,19], sodium metal anodes have limited large-scale applicability due to the safety concerns caused by dendrites. Though having large storage capacities, other elements of group 14 and 15, such as Si, Sn, P etc., suffer from major volume changes and other shortcomings [20,21]. When compared to other materials, carbon-based materials have received more widespread attention due to their low-cost, high structural stability, and flexibility [22,23]. Specifically, the large surface area and high electronic conductivity are important for inhibiting the formation of dendrites [24,25]. Many carbon materials, including graphite [26], hard carbon [27], hollow carbon nanospheres [28], and graphene [29], have demonstrated feasibility and potential as SIB anode materials. Note that the N-doped graphene foams synthesized by Dai's group in 2015 was reported to have the largest storage capacity (852.6 mAh/g) up to now [30]. This work strongly demonstrates the well-defined carbon materials could have competing capacity to the LIBs. However, some shortcomings, especially with the small benzene rings in sp^2 carbon, can induce poor rate capacities. [31]. In view of these efforts, development of a carbon material with large holes and large specific surface area has become key to solving these issues.

In 1987, Baughman et al. predicted a two-dimensional material with both sp- and sp^2-hybridized carbon atoms, which was named graphyne (Gy) [32]. Li's group first realized the synthesis of large-scale graphdiyne in 2010 [33]. Gy has abundant carbon chemical bonds, large conjugated systems, wide interplanar spacing, and excellent chemical stability. In the past decade, graphyne has become a hot issue in many application fields [34,35]. Especially in the field of ion batteries, where graphyne exhibits several advantages, including high specific capacity, excellent rate performance, and stability [36,37]. Recently, graphyne materials have received growing attention as potential SIB anodes. In 2017, Huang et al. reported a three-dimensional graphdiyne nanosheet as anode materials, which delivers a stable reversible capacity of 812 mAh/g at a current density of 0.05 A/g [38]. In 2019, they further reported well-defined hydrogen-substituted graphyne (HsGY) with a reversible capacity of 600 mAh/g at a current density of 100 mA/g [37]. In 2020, Cui's group synthesized N-doped γ-graphyne (NGY) to deliver a large reversible storage capacity of 570.4 mAh/g at 100 mA/g, accompanied by excellent rate capability [39]. Through a first principles investigation, Xu et al. determined that graphyne and graphdiyne have not only high Na storage capacity, but also strong diffusions because of the existence of large sized pores [40]. These studies have demonstrated graphyne-related materials as potential SIB anode materials.

Formation of graphyne nanotubes (GyNTs) is one of many modification methods of graphyne. At present, many studies have confirmed that rolling 2D graphyne into nanotubes can significantly modify their structural and electronic properties [23,41,42]. We have reported that γGyNTs could be promising LIB anode materials as they have a predicted maximum lithium storage capacity of 2232 mAh/g [41]. It was discovered that the curvature of γGyNTs has great influence on the storage and migration of lithium. Thus, we believe GyNTs are promising candidates for next-generation SIB anode materials due to their large, conjugated, structure-adjustable curvature, and larger number of possible active sites. In addition, many graphyne-based materials including graphdiyne nanoribbons [42] and graphdiyne nanotubes [43] have been successfully synthesized, which makes us expect the realization of GyNTs in near future. Therefore, in the present study, we investigate the performance of GyNTs as SIB anode materials through density functional theory calculations. We calculate the maximum Na storage specific capacity of GyNTs with different radii and obtained the maximum specific capacities using binding energies, open circuit voltages, and structural characteristics. Our results show that all studied GyNTs have better maximum specific capacities than a single-layer Gy. Specifically, (3, 0)-αGyNT, (2, 2)-βGyNT, and (4, 0)-γGyNT, were predicted to have the best storage capacities of each type of graphyne, with values of 1535, 1302, and 1001 mAh/g, respectively. Our results further suggest that large hexagonal pores could resolve the transportation problem caused by the large atomic radius of sodium.

2. Computational Method

In this study, all density functional theory (DFT) calculations were implemented by the Vienna Ab Initio Simulation Package (VASP) with a projector-augmented wave (PAW) method [44]. The exchange–correlation functional was used with the generalized gradient approximation (GGA) in the Perdew–Burke–Ernzerhof (PBE) scheme [45], coupling with spin polarization. The cutoff energy was set to 400 eV, and the geometries were optimized until no residual force acting on any atom exceeded 0.05 eV/Å, and the energy change was less than 10^{-4} eV. We applied each unit cell of the α, β and γGyNTs as a substrate to adsorb Na. The first Brillouin zone integration was conducted using the Monkhorst–Pack scheme with a *k*-point sampling of $1 \times 1 \times 4$ [46], where the *c* axis was set as the periodic direction. The optimal structures of all studied GyNTs are available in the electronic supplementary information (ESI, Figures S1–S3). Therefore, we can determine the diffusion paths and diffusion energy barriers of Na atoms on GyNTs using the climbing-image-nudged-elastic-band (CI-NEB) [47].

The adsorption strength can be indicated by the binding energy (E_b) of Na atoms on every GyNT, which is defined below:

$$E_b = (E_{C\text{-}Na} - E_C - NE_{Na})/N \quad (1)$$

where N is the total number of Na atoms adsorbed on the GyNT, $E_{C\text{-}Na}$ is the total energy of Na atom(s) adsorbed on the GyNT, E_C is the energy of the substrate GyNT, and E_{Na} is the energy of an isolated Na atom in a vacuum.

To obtain the open-circuit voltage (V_{OCV}) of the SIB anode materials, the following formula can be applied [36]:

$$V_{OCV} = -\frac{\Delta G}{\Delta Ne} \quad (2)$$

where ΔG is the difference in Gibbs free energy, ΔN is the difference in the number of Na ions at two compositions during charging/discharging, and e is the electronic charge of the Na ions (e = 1).

$$\Delta G = \Delta E + P\Delta V - T\Delta S \quad (3)$$

because the contribution of the volume and entropy terms are negligible, ΔG can be approximated as ΔE [48]. Therefore, V_{OCV} can be simplified to the following formula:

$$V_{OCV} = (E_C + NE_{bcc\text{-}Na} - E_{C\text{-}Na})/\Delta Ne \quad (4)$$

where $E_{bcc\text{-}Na}$ is the energy of one Na atom in body-centered cubic (bcc) form. The E_b and V_{OCV} of Na atoms adsorbed on a GyNT were calculated as a function of Na concentration x, where x is defined from C_6Na_x. Taking (3, 0)-αGyNT for instance, $N = 8x$, so that $C_{48}Na_N$ is reduced to C_6Na_x.

3. Results and Discussion

3.1. Single Na Adsorption on GyNTs

First, we studied the adsorption of a single Na atom on 2D graphyne films. For αGy, the single Na atom prefers to be adsorbed at the center of the hexagonal acetylenic ring (H_α), as shown in Figure 1a. The distance between the Na and the sp-C atom ($R_{C\text{-}Na}$) is about 2.70 Å, and the E_b was computed to be −2.02 eV by Equation 1. In contrast, βGy has two sites that anchor the Na atom, the centers of the hexagonal acetylenic ring, and the triangular acetylenic ring (denoted as H_β and h_β, respectively). The optimized structures at H_β and h_β are presented in Figure 1b, which shows $R_{C\text{-}Na}$ values of 2.69 Å and 2.64 Å, with E_b values of −2.25 and −2.30 eV, respectively. Similarly, γGy also has two Na sites: the centers of hexagonal acetylenic ring and benzene ring (denoted as H_γ and h_γ, respectively). The E_b values at H_γ and h_γ were computed to be −2.08 and −1.45 eV, respectively. The E_b at H_γ is more negative than that at h_γ because of its larger size, as shown in Figure 1c. Our results, consistent with the previous results of Xu et al. [40], indicate that the three

Gy models can anchor a Na atom because the cohesive energy (E_{coh}) of bulk Na is only −1.04 eV.

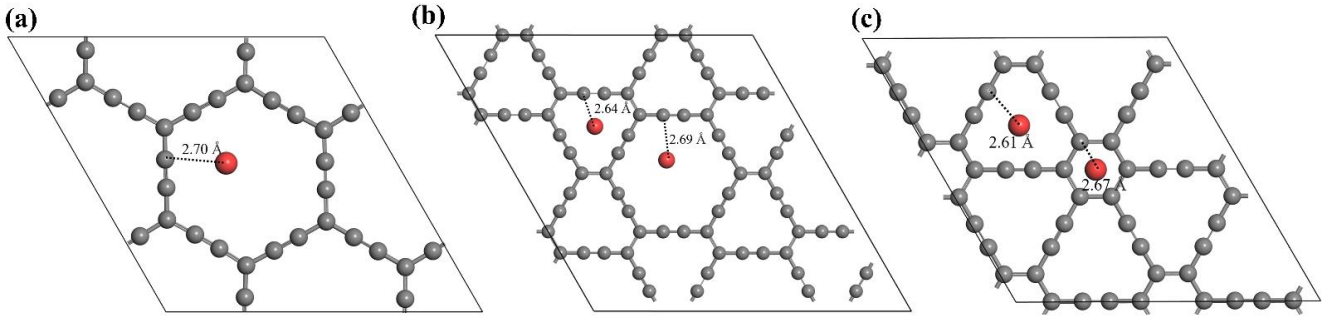

Figure 1. Optimized structures of a single Na atom adsorbed in 2D (**a**) αGy, (**b**) βGy, and (**c**) γGy.

Next, we explored the adsorption of a single Na on GyNTs. Our previous work suggested that curvature can cause differentiations of sp- and sp^2-C atoms [41], inducing more possible adsorption sites. These sites include the top site (t) on single C atoms, the bridge site (b) between two bonded C atoms, and the hollow sites of acetylenic rings (denoted H or h depending on pore size), as illustrated in Figure 2. We used the superscript (′) to represent concave cases. A Na atom was placed at these positions at initial distances of about 1.8 Å, and full relaxations were performed. For αGyNTs, there is no distinction between H_α and H_α′ because the hexagonal acetylenic rings are large enough to anchor a Na at the center regardless of tube size (n). Figure 3a shows the E_b of a single Na on αGyNTs as a function of tube size (n). The E_b values of both (n, n) and (n, 0)-αGyNTs increases with tube size, gradually converging to −2.02 eV. It is also evident that the E_b values of both (n, n)-αGyNTs are always larger than that of (n, 0)-αGyNTs because (n, n)αGyNTs have a larger radius.

Similar to the Na adsorption on αGyNTs, H_β and H_β'coincide because of the large size of the hexagonal acetylenic rings of all βGyNTs. As shown in Figure 3b, the E_b values at H_β and h_β, regardless of the curvature, show V-shaped behaviors, and are predicted to converge to that of 2D βGy. Furthermore, there is an interesting phenomenon that the most stable adsorption position varies with tube radius. When r < 5.23 Å, the most stable adsorption site is H_β; when 5.23 Å < r < 7.835 Å, the most stable adsorption site is h_β; when r > 7.835 Å, the most stable adsorption site is h_β′.

Next, we studied Na adsorption on γGyNTs. The E_b of single Na is −1.81/−1.82, −1.83/−1.82, and −1.86/−1.86 eV/Na at the H_γ/H_γ′ site for (n, n)-γGyNTs and −1.70/−1.71, −1.94/−1.91, and −1.88/−1.87 eV/Na at the H_γ/H_γ′ site for (n, 0)-γGyNTs, respectively. Figure 3c shows the E_b values at H_γ, H_γ′, h_γ, and h_γ′ as a function of tube size (n). The E_b at the H_γ (H_γ′) site is always larger than that at the h_γ (h_γ′) site, and the H_γ is always the most favored site. The E_b at the H_γ (H_γ′) site monotonically decreases with tube size on (n, n)-γGyNTs; however, it first increases, then decreases with tube size on (n, 0)-γGyNTs.

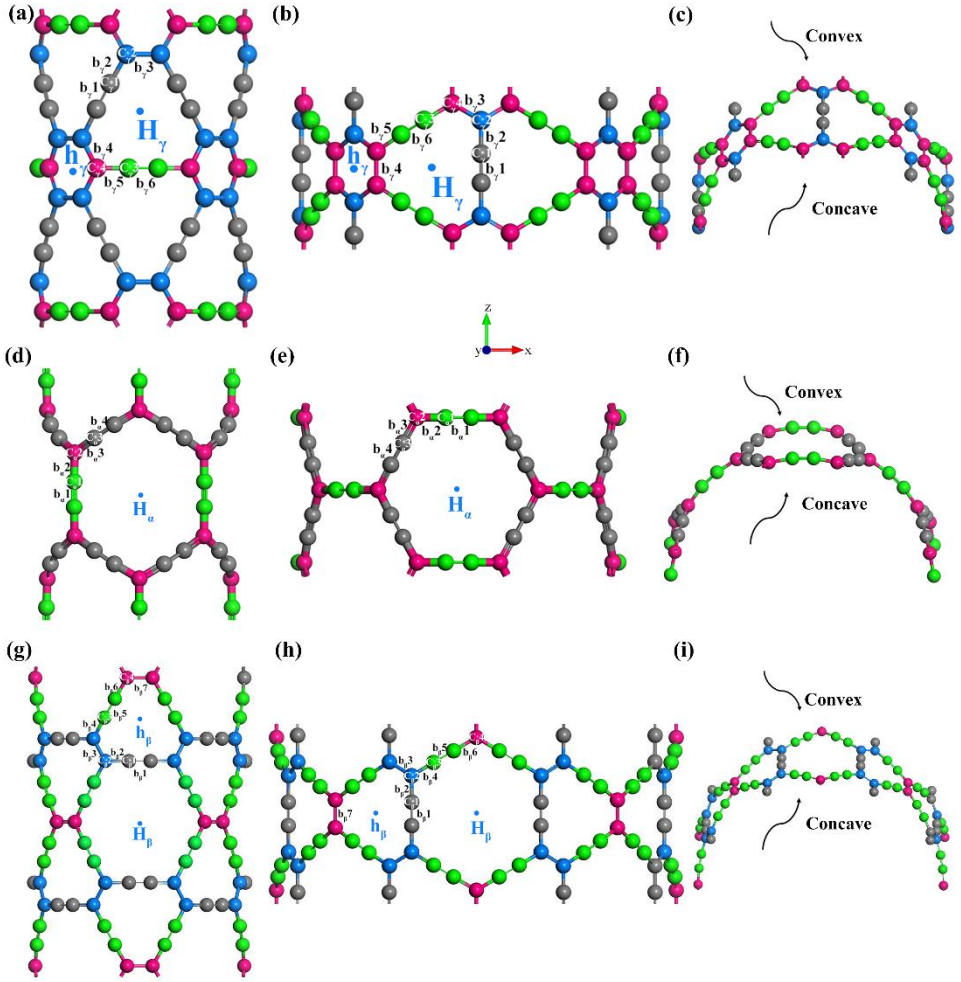

Figure 2. Illustration of possible adsorption sites for a single Na atom on (**a**) (*n*, 0)-γGyNTs, (**b**) (*n*, *n*)-γGyNTs, (**d**) (*n*, 0)-αGyNTs, (**e**) (*n*, *n*)-αGyNTs, (**g**) (*n*, 0)-βGyNTs, and (**h**) (*n*, *n*)-βGyNTs. The convex and concave positions of (**c**) γGyNTs, (**f**) αGyNT, and (**i**) βGyNTs (Pink: sp^2-C with large curvature; blue: sp^2-C with small curvature; green: sp-C with large curvature; grey: sp-C with small curvature).

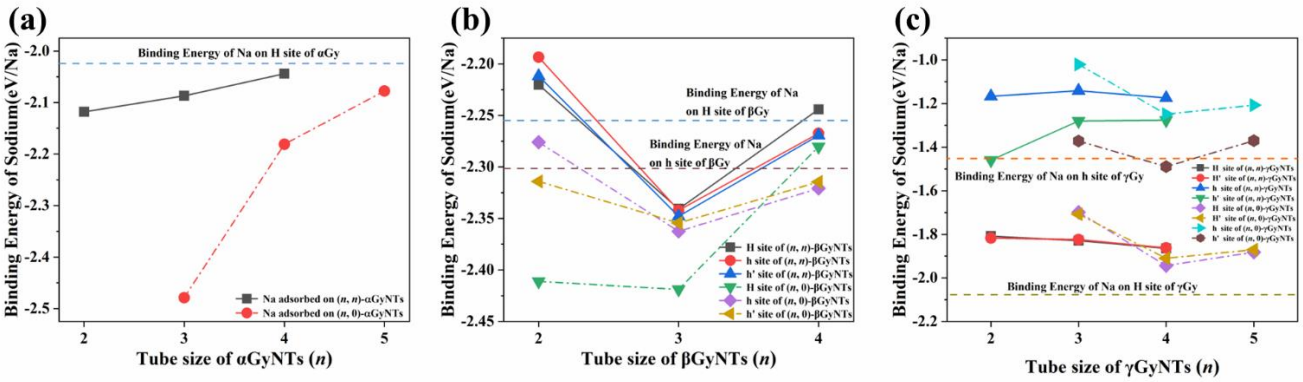

Figure 3. The change of E_b of single Na as a function of tube size for (**a**) αGyNTs, (**b**) βGyNTs, and (**c**) γGyNTs.

3.2. Sodium Storage Capacity of GyNTs

In order to explore the maximum storage capacity, we gradually introduced more Na atoms into single-layered Gy films and GyNTs. The changes to E_b and V_{OCV} were computed as a function of Na concentration x, which was set as 0 when only a single Na atom was

considered for simplicity. Figure 4 shows the changes to E_b and V_{OCV} as a function of Na concentration x. The C_{max}^{Na} values of 2D αGy, βGy, and γGy were determined to be $C_6Na_{1.5}$, $C_6Na_{1.0}$, and $C_6Na_{1.5}$. When reaching the C_{max}^{Na}, the corresponding E_b values were −1.35, −1.08, and −1.56 eV/Na, and the V_{OCV} values were 0.014, 0.29 and 0.49 V by Equation 4 as shown in Figure 4. The optimized structures shown in Figure S4 indicate that all Na atoms are anchored and stable since all $R_{C\text{-}Na}$ are about 2.7 Å. Therefore, the maximum specific capacities of αGy, βGy, and γGy, are 558, 372, and 558 mAh/g, respectively. It is notable that a previous study reported the maximum specific capacity of γGy to be 558 mAh/g [40], which is consistent with our results, indicating the reliability of our calculations.

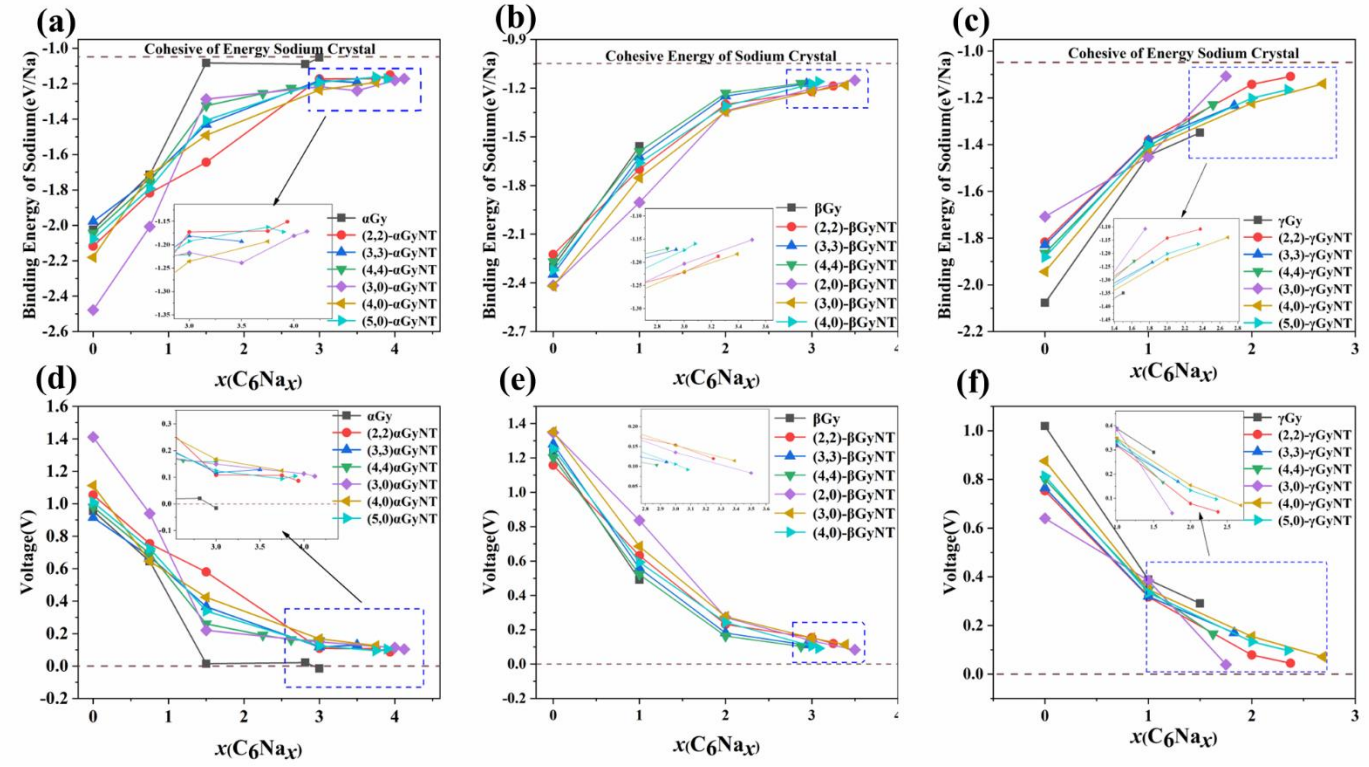

Figure 4. The changes to E_b of (**a**) α, (**b**) β, and (**c**) γGyNTs as a function of the Na concentration x, and V_{OCV} as a function of Na concentration x of (**d**) α, (**e**) β, and (**f**) γGyNTs.

When the 2D Gy is curled seamlessly into a GyNT, the C_{max}^{Na} changes significantly, as revealed in prior work. The changes to E_b and V_{OCV} as a function of the Na concentration x of αGyNTs are shown in Figure 4a,d. For (n, n)-αGyNTs, the C_{max}^{Na} values were computed to be $C_6Na_{3.94}$, $C_6Na_{3.50}$, and $C_6Na_{3.00}$ when n = 2, 3, and 4, respectively, and the corresponding E_b and V_{OCV} values are −1.15, −1.19, and −1.22 eV/Na and 0.12, 0.11, and 0.10 V, respectively. For (n, 0)-αGyNTs, the predicted C_{max}^{Na} values are $C_6Na_{4.13}$, $C_6Na_{3.75}$, and $C_6Na_{3.53}$ when n = 3, 4, and 5, and their corresponding E_b and V_{OCV} values were −1.17, −1.19, and −1.19 eV/Na and 0.08, 0.11, and 0.09 V, respectively. To confirm the maximum sodium storage capacity of αGyNTs, we checked the optimized structure of (3, 0)-αGyNT with C_{max}^{Na} as shown in Figure 5a, while the data for other αGyNTs are available in Figure S5. We discovered that every Na atom directly interacts with the C atoms of αGyNTs. Therefore, the maximum Na storage capacity of αGyNTs is $C_6Na_{4.125}$ (1535 mAh·g^{-1}).

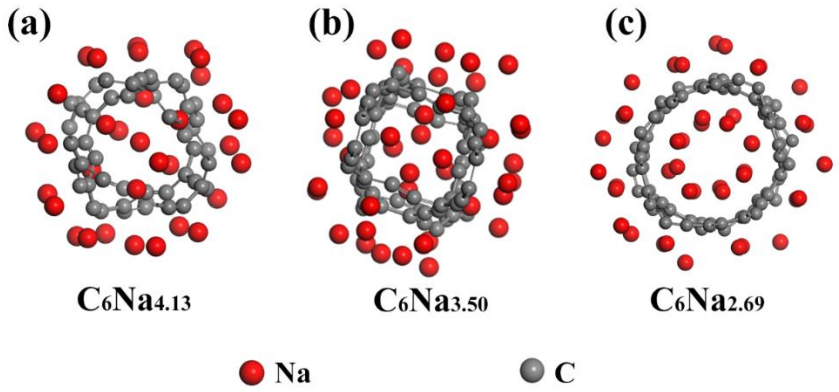

Figure 5. Optimized geometries with maximum storage capacity of (**a**) (3, 0)-αGyNT, (**b**) (2, 0)-βGyNT and (**c**) (4, 0)-γGyNT.

Following the same approach, we tried to determine the C_{max}^{Na} values of the studied βGyNTs. The changes of E_b and V_{OCV} as functions of the Na concentration x of βGyNTs is shown in Figure 4b,e. For (n, n)-βGyNTs, the expected C_{max}^{Na} values are $C_6Na_{3.25}$, $C_6Na_{2.94}$, and $C_6Na_{2.88}$ when n = 2, 3, and 4, respectively, and the E_b and V_{OCV} values are −1.18, −1.18, and −1.17 eV/Na and 0.12, 0.11, and 0.10 V, respectively, when the GyNTs reach the expected maximum storage capacity. For (n, 0)-βGyNTs, the expected C_{max}^{Na} are $C_6Na_{3.50}$, $C_6Na_{3.39}$, and $C_6Na_{3.08}$ when n = 2, 3, and 4, respectively. The corresponding E_b and OCV values are −1.15, −1.18, and −1.16 eV/Na and 0.08, 0.11, and 0.09 V for the (n, 0)-βGyNTs. Moreover, we also checked the optimized geometries with the maximum storage capacity of βGyNTs, as shown in Figure 5b and Figure S6. Thus, the maximum storage Na capacity of βGyNTs is $C_6Na_{4.125}$ (1535 mAh·g^{-1}).

The changes to E_b and OCV as a function of Na concentration x of γGyNTs are shown in Figure 4c,f. For (n, n)-γGyNTs, when n = 2, 3, and 4, respectively, the expected C_{max}^{Na} were computed to be $C_6Na_{2.38}$, $C_6Na_{1.83}$, and $C_6Na_{1.63}$, with corresponding E_b and V_{OCV} values of −1.11, −1.23, and −1.23 eV/Na and 0.04, 0.17, and 0.16 V, respectively. For (n, 0)-γGyNTs, when n = 3, 4, and 5, the C_{max}^{Na} are expected to be $C_6Na_{1.75}$, $C_6Na_{2.69}$, $C_6Na_{2.23}$, respectively, and the E_b and V_{OCV} values are −1.11, −1.14, and −1.16 eV/Na and 0.04, 0.07, and 0.10 V, respectively. As shown in Figure 5c and Figure S7, as the structures approached C_{max}^{Na}, the distance of every Na to its nearest C atom was 2.65~2.74 Å, indicating that every Na atom can strongly bind to the γGyNTs via a chemical bond. Thus, the maximum storage Na capacity of γGyNTs is $C_6Na_{4.13}$ (1535 mAh·g^{-1}).

Figure 6a shows the variations of maximum storage capacity as a function of tube size (n) for all studied GyNTs. It is evident that, as n increases, the C_{max}^{Na} values monotonically decrease, except for those of (3, 0)-γGyNT. Furthermore, the C_{max}^{Na} of (n, 0)-GyNTs is greater than those of corresponding (n, n)-GyNTs with the same n, which is ascribed to the smaller radii of (n, 0)-GyNTs than (n, n)-GyNTs. The distinct behavior of (3, 0)-γGyNT also originates from its smallest radius, which limits the storage of Na on the inner side. Therefore, we plotted the change of maximum storage capacity as a function of tube radius (r) in Figure 6b. It is worth noting that the tube radius and the maximum capacity present an excellent correlation for all α, β, and γGyNTs. The tube radius is an important determining factor of maximum capacity: a smaller tube radius leads to a larger area exposed by π-π conjugation on the convex side of the GyNTs, which makes it more capable of adsorbing Na atoms. Furthermore, the C_{max}^{Na} of αGyNTs is always the largest, and that of γGyNTs is always smallest for a given radius, which should originate from the difference in specific surface area. The specific surface areas of 2D α, β, and γGy are 21,089, 17,321, and 13,732 m^2/g, respectively.

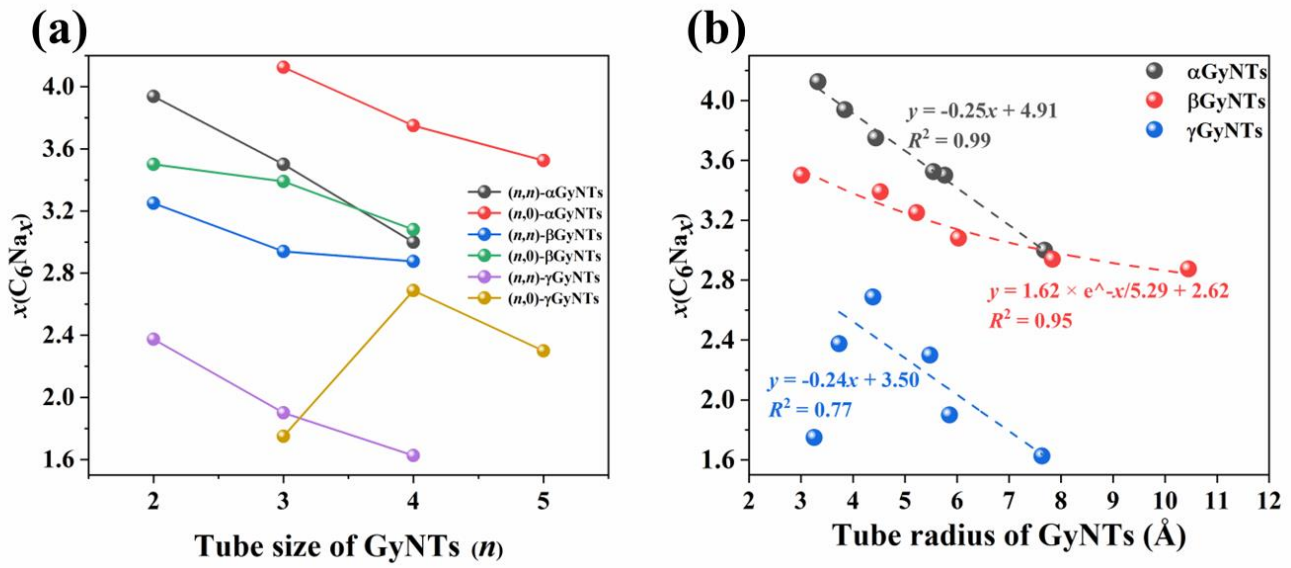

Figure 6. The changes of maximum storage capacity as a function of (**a**) tube size and (**b**) tube radius.

3.3. Sodium Diffusion and Migration on GyNTs

For the GyNTs to be an excellent SIB anode, they must have not only a high specific capacity, but also a great rate performance. Herein, we calculated the diffusion path and migration energy barriers of Na on the convex and concave surfaces of (3, 0)-αGyNT, (2,0)-βGyNT, and (4, 0)-γGyNT, which exhibited the best Na storage ability of each GyNT type. For comparison, the Na diffusion on 2D Gy films was explored in advance. Figure S8a shows the calculated energy profile of Na diffusion along the favored path on αGy, and the energy barrier ($\Delta E^{\ddagger}$) was computed to be 0.535 eV. Na diffusion on (3, 0)-αGyNTs will have more diffusion paths than that on αGy. We calculated the $\Delta E^{\ddagger}$ of the favored diffusion path, $H_0 \rightarrow H_1 \rightarrow H_2$ for the convex surface and $H_{0'} \rightarrow H_{1'} \rightarrow H_{2'}$ for the concave surface, as illustrated in Figure 7a,b. For the convex path, the $\Delta E^{\ddagger}$ of $H_0 \rightarrow H_1$, $H_1 \rightarrow H_2$, and $H_2 \rightarrow H_0$ are, respectively, 0.818, 0.779, and 0.785 eV, which are slightly higher than that on αGy. On the concave path, the $\Delta E^{\ddagger}$ values of $H_{0'} \rightarrow H_{1'}$, $H_{1'} \rightarrow H_{2'}$, and $H_{2'} \rightarrow H_{0'}$ significantly decrease to 0.047, 0.049, and 0.057 eV, respectively.

Figure S8b exhibits the Na diffusion on 2D βGy, for which the $\Delta E^{\ddagger}$ of diffusion paths $h_1 \rightarrow h_2$, $h_2 \rightarrow h_3$, $h_3 \rightarrow H$, and $H \rightarrow h_1$ are 0.549, 0.685, 0.662, and 0505 eV, respectively. The maximum $\Delta E^{\ddagger}$ of Na on βGy is larger than that on αGy because βGy has a stronger adsorption capacity for Na. For Na on (2, 0)-βGyNTs, the simulated diffusion pathways are displayed in Figure 7c,d. The $\Delta E^{\ddagger}$ values of $h_1 \rightarrow h_2$, $h_2 \rightarrow h_3$, $h_3 \rightarrow H$, and $H \rightarrow h_1$ are 0.657, 0.727, 0.626, and 0.717 eV, respectively, whereas those of $h_{1'} \rightarrow h_{2'}$, $h_{2'} \rightarrow h_{3'}$, $h_{3'} \rightarrow H'$, and $H' \rightarrow h_{1'}$ are 0.089, 0.174, 0.093, and 0.100 eV. Figure S8c shows the Na diffusion on the 2D γGy, which has two diffusion paths, $H_1 \rightarrow H_2$ and $H_2 \rightarrow h$, with $\Delta E^{\ddagger}$ values of 0.543 and 0.681 eV, respectively. For Na on (4, 0)-γGyNT, schematic drawings of the diffusion path and energy profiles are shown in Figure 7e,f. The $\Delta E^{\ddagger}$ values on the convex and concave surfaces are 0.687, 0.591, 0.798, and 0.120 eV and 0.214, 0.352, 0.420, and 0.010 eV, respectively.

For all studied GyNTs, the $\Delta E^{\ddagger}$ on the concave surface is much smaller than that on convex surface, which has to be attributed to the curvature effect that was discussed thoroughly in the previous study [41]. Thus, we conclude that GyNTs can provide good channels for diffusion of Na, and the $\Delta E^{\ddagger}$ on αGy(NTs) and βGy(NTs) are smaller than that on γGy(NTs). Moreover, in addition to diffusion, the penetration of Na through GyNTs is another important factor for rate performance. For αGy(NTs) and βGy(NTs), the large size of the hexagonal acetylenic rings promises easy penetration. In contrast, the pore sizes of γGy(NTs) are smaller than those of the other two types, which can inhibit penetration of Na. Figure S8d shows the Na penetrating γGy through H, whose $\Delta E^{\ddagger}$ is up to 1.382 eV.

Relatively speaking, αGy(NTs) and βGy(NTs) should have better rate performance than γGy(NTs).

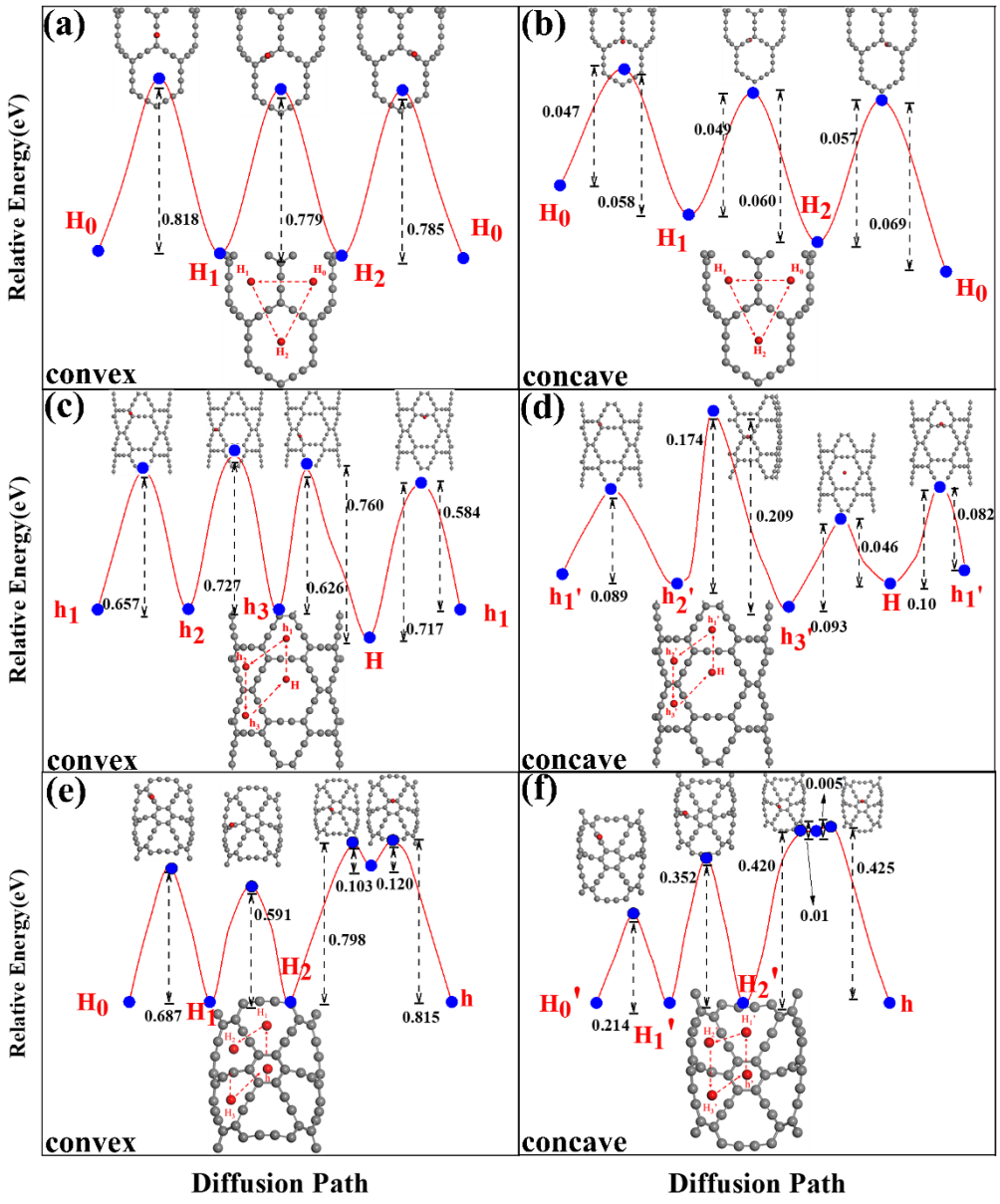

Figure 7. Schematics of the diffusion path and energy profiles for a sodium-ion on (**a**,**b**) (3, 0)-αGyNT, (**c**,**d**) (2, 0)-βGyNT, and (**e**,**f**) (4, 0)-γGyNT.

4. Conclusions

In summary, by carrying out density functional theory calculations, we investigated the applicability of α, β, and γ graphyne nanotubes (αGyNTs, βGyNTs, and γGyNTs, respectively) as SIB anodes. We predicted the maximum storage capacity of every studied graphyne nanotube by calculating the average binding energy and open-circuit voltage. The maximum storage capacity of every type of nanotube monotonically decreases with increases to the tube's radius. The (3, 0)-αGyNT, (2, 2)-βGyNT, and (4, 0)-γGyNT had the maximum Na storage capacities of 1535, 1302, and 1001 mAh/g, respectively, for each type of GyNT. These values significantly exceed the largest reported values (N-doped graphene foams with 852.6 mAh/g capacity) in carbon materials. It was discovered that αGyNT has the largest, while γGyNT has the smallest storage capacity for a given tube size, which is ascribed to the fact that αGyNTs possess the larger specific surface area. The

NEB calculations reveal that Na ions can diffuse more easily into concave surfaces than on convex surfaces on a 2D film, which can promote migration of Na ions. Additionally, the large hexagonal acetylenic link can allow Na ions to easily penetrate, which can promote the diffusivity of Na ions. Overall, our results suggest that αGyNTs and βGyNTs are potential candidates as SIB anodes with ultra-high storage capacities and promising rate capabilities. Our study significantly enlarges the applicable field of graphyne materials.

Supplementary Materials: The following supporting information can be downloaded at: https://www.mdpi.com/article/10.3390/catal12060670/s1, Figure S1: Optimized structure of all studied αGyNTs; Figure S2: Optimized structure of all studied βGyNTs; Figure S3: Optimized structure of all studied γGyNTs.; Figure S4: Optimized structure of αGy (a), βGy (b), and γGy (c) when reaching the maximum storage Na capacities; Figure S5: Optimized geometries with maximum storage capacity of (a) (2, 2)-αGyNT, (b) (3, 3)-αGyNT, (c) (4, 4)-αGyNT, (d) (4, 0)-αGyNT, and (e) (5, 0)-αGyNT; Figure S6: Optimized geometries with maximum storage capacity of (a) (2, 2)-βGyNT, (b) (3, 3)- βGyNT, (c) (4, 4)-βGyNT, (d) (3, 0)- βGyNT, and (e) (4, 0)-βGyNT; Figure S7: Optimized geometries with maximum storage capacity of (a) (2, 2)-γGyNT, (b) (3, 3)-γGyNT, (c) (4, 4)-γGyNT, (d) (3, 0)-γGyNT, and (e) (5, 0)-γGyNT; Figure S8: Energy surfaces of Na diffusion on (a) αGy, (b) βGy, (c) γGy, and Na penetrates on (d) γGy.

Author Contributions: Conceptualization, B.K.; formal analysis, Y.Y., J.M., Y.C. and X.S.; investigation, Y.Y. and X.S.; resources, F.W.; data curation, Y.Y. and X.S.; writing—original draft preparation, Y.Y. and X.S.; writing—review and editing, B.K. and J.Y.L.; supervision, B.K. and J.Y.L.; project administration, J.Y.L.; funding acquisition, B.K. and J.Y.L. All authors have read and agreed to the published version of the manuscript.

Funding: This research was funded by the National Natural Science Foundation of China (21803023). J.Y.L. acknowledges financial support from a National Research Foundation (NRF) grant funded by the Korean government (2019R1A6A1A10073079 and 2022R1A4A1032832).

Institutional Review Board Statement: Not applicable.

Informed Consent Statement: Not applicable.

Data Availability Statement: The data presented in this study are available on request from the corresponding author.

Conflicts of Interest: The authors declare no conflict of interest.

References

1. Tarascon, J.M. Is lithium the new gold? *Nat. Chem.* **2010**, *2*, 510. [CrossRef]
2. Dunn, B.; Kamath, H.; Tarascon, J.M. Electrical energy storage for the grid: A battery of choices. *Science* **2011**, *334*, 928–935. [CrossRef] [PubMed]
3. Whittingham, M.S. Electrical energy storage and intercalation chemistry. *Science* **1976**, *192*, 1126–1127. [CrossRef] [PubMed]
4. Tarascon, J.M.; Armand, M. Issues and challenges facing rechargeable lithium batteries. *Nature* **2001**, *414*, 359–367. [CrossRef] [PubMed]
5. Kong, H.; Lv, C.; Wu, Y.; Yan, C.; Chen, G. Integration of cobalt selenide nanocrystals with interlayer expanded 3D Se/N Co-doped carbon networks for superior sodium-ion storage. *J. Energy Chem.* **2021**, *55*, 169–175. [CrossRef]
6. Pan, H.L.; Hu, Y.S.; Chen, L.Q. Room-temperature stationary sodium-ion batteries for large-scale electric energy storage. *Energy Environ. Sci.* **2013**, *6*, 2338–2360. [CrossRef]
7. Palomares, V.; Serras, P.; Villaluenga, I.; Hueso, K.B.; Carretero-González, J.; Rojo, T. Na-ion batteries, recent advances and present challenges to become low cost energy storage systems. *Energy Environ. Sci.* **2012**, *5*, 5884–5901. [CrossRef]
8. Zhu, C.; Mu, X.; van Aken, P.A.; Yu, Y.; Maier, J. Single-Layered Ultrasmall Nanoplates of MoS2 Embedded in Carbon Nanofibers with Excellent Electrochemical Performance for Lithium and Sodium Storage. *Angew. Chem. Int. Ed.* **2014**, *53*, 2152–2156. [CrossRef] [PubMed]
9. Hwang, J.Y.; Myung, S.T.; Sun, Y.K. Sodium-ion batteries: Present and future. *Chem. Soc. Rev.* **2017**, *46*, 3529–3614. [CrossRef]
10. Lee, B.; Paek, E.; Mitlin, D.; Lee, S.W. Sodium Metal Anodes: Emerging Solutions to Dendrite Growth. *Chem. Rev.* **2019**, *119*, 5416–5460. [CrossRef]
11. Zheng, X.Y.; Bommier, C.; Luo, W.; Jiang, L.H.; Hao, Y.N.; Huang, Y.H. Sodium metal anodes for room-temperature sodium-ion batteries: Applications, challenges and solutions. *Energy Storage Mater.* **2019**, *16*, 6–23. [CrossRef]
12. Dou, X.W.; Hasa, I.; Saurel, D.; Vaalma, C.; Wu, L.M.; Buchholz, D.; Bresser, D.; Komaba, S.; Passerini, S. Hard carbons for sodium-ion batteries: Structure, analysis, sustainability and electrochemistry. *Mater. Today* **2019**, *23*, 87–104. [CrossRef]

13. Jiang, H.; Gu, J.X.; Zheng, X.S.; Liu, M.; Qiu, X.Q.; Wang, L.B.; Li, W.Z.; Chen, Z.F.; Ji, X.B.; Li, J. Defect-rich and ultrathin N doped carbon nanosheets as advanced trifunctional metal-free electrocatalysts for the ORR, OER and HER. *Energy Environ. Sci.* **2019**, *12*, 322–333. [CrossRef]
14. Xia, J.; Liu, L.; Jamil, S.; Xie, J.J.; Yan, H.X.; Yuan, Y.T.; Zhang, Y.; Nie, S.; Pan, J.; Wang, X.Y.; et al. Free-standing SnS/C nanofiber anodes for ultralong cycle-life lithium-ion batteries and sodium-ion batteries. *Energy Storage Mater.* **2019**, *17*, 1–11. [CrossRef]
15. Fang, G.Z.; Wang, Q.C.; Zhou, J.; Lei, Y.P.; Chen, Z.X.; Wang, Z.Q.; Pan, A.Q.; Liang, S.Q. Metal organic framework-templated synthesis of bimetallic selenides with rich phase boundaries for Sodium-Ion storage and oxygen evolution reaction. *ACS Nano* **2019**, *13*, 5635–5645. [CrossRef] [PubMed]
16. Liu, Y.; Fang, Y.J.; Zhao, Z.W.; Yuan, C.Z.; Lou, X.W. A ternary Fe1-xS@porous carbon nanowires/reduced graphene oxide hybrid film electrode with superior volumetric and gravimetric capacities for flexible sodium ion batteries. *Adv. Energy Mater.* **2019**, *9*, 1803052. [CrossRef]
17. Wang, L.; Wei, Z.X.; Mao, M.L.; Wang, H.X.; Li, Y.T.; Ma, J.M. Metal oxide/graphene composite anode materials for sodium-ion batteries. *Energy Storage Mater.* **2019**, *16*, 434–454. [CrossRef]
18. Luo, W.; Hu, L. Na Metal Anode: "Holy Grail" for Room-Temperature Na-Ion Batteries? *ACS Cent. Sci.* **2015**, *1*, 420–422. [CrossRef]
19. Hartmann, P.; Bender, C.L.; Vračar, M.; Dürr, A.K.; Garsuch, A.; Janek, J.; Adelhelm, P. A rechargeable room-temperature sodium superoxide (NaO_2) battery. *Nat. Mater.* **2013**, *12*, 228–232. [CrossRef]
20. Yabuuchi, N.; Kubota, K.; Dahbi, M.; Komaba, S. Research Development on Sodium-Ion Batteries. *Chem. Rev.* **2014**, *114*, 11636–11682. [CrossRef]
21. Kang, H.Y.; Liu, Y.C.; Cao, K.Z.; Zhao, Y.; Jiao, L.F.; Wang, Y.J.; Yuan, H.T. Update on anode materials for Na-ion batteries. *J. Mater. Chem. A* **2015**, *3*, 17899–17913. [CrossRef]
22. Saurel, D.; Orayech, B.; Xiao, B.; Carriazo, D.; Li, X.; Rojo, T. From Charge Storage Mechanism to Performance: A Roadmap toward High Specific Energy Sodium-Ion Batteries through Carbon Anode Optimization. *Adv. Energy Mater.* **2018**, *8*, 1703268. [CrossRef]
23. Kang, B.; Moon, J.H.; Lee, J.Y. Size dependent electronic band structures of beta- and gamma-graphyne nanotubes. *RSC Adv.* **2015**, *5*, 80118–80121. [CrossRef]
24. Lu, L.L.; Ge, J.; Yang, J.N.; Chen, S.M.; Yao, H.B.; Zhou, F.; Yu, S.H. Free-Standing Copper Nanowire Network Current Collector for Improving Lithium Anode Performance. *Nano Lett.* **2016**, *16*, 4431–4437. [CrossRef] [PubMed]
25. Zhang, R.; Cheng, X.B.; Zhao, C.Z.; Peng, H.J.; Shi, J.L.; Huang, J.Q.; Wang, J.; Wei, F.; Zhang, Q. Conductive Nanostructured Scaffolds Render Low Local Current Density to Inhibit Lithium Dendrite Growth. *Adv. Mater.* **2016**, *28*, 2155–2162. [CrossRef]
26. Wen, Y.; He, K.; Zhu, Y.J.; Han, F.D.; Xu, Y.H.; Matsuda, I.; Ishii, Y.; Cumings, J.; Wang, C.S. Expanded graphite as superior anode for sodium-ion batteries. *Nat. Commun.* **2014**, *5*, 4033. [CrossRef]
27. Jian, Z.L.; Xing, Z.Y.; Bommier, C.; Li, Z.F.; Ji, X.L. Hard Carbon Microspheres: Potassium-Ion Anode Versus Sodium-Ion Anode. *Adv. Energy Mater.* **2016**, *6*, 1501874. [CrossRef]
28. Tang, K.; Fu, L.J.; White, R.J.; Yu, L.H.; Titirici, M.M.; Antonietti, M.; Maier, J. Hollow Carbon Nanospheres with Superior Rate Capability for Sodium-Based Batteries. *Adv. Energy Mater.* **2012**, *2*, 873–877. [CrossRef]
29. Ma, C.; Xu, T.; Wang, Y. Advanced carbon nanostructures for future high performance sodium metal anodes. *Energy Storage Mater.* **2020**, *25*, 811–826. [CrossRef]
30. Xu, J.T.; Wang, M.; Wickramaratne, N.P.; Jaroniec, M.; Dou, S.X.; Dai, L.M. High-Performance Sodium Ion Batteries Based on a 3D Anode from Nitrogen-Doped Graphene Foams. *Adv. Mater.* **2015**, *27*, 2042–2048. [CrossRef]
31. Zhang, S.; He, J.; Zheng, J.; Huang, C.; Lv, Q.; Wang, K.; Wang, N.; Lan, Z. Porous graphdiyne applied for sodium ion storage. *J. Mater. Chem. A* **2016**, *5*, 2045–2051. [CrossRef]
32. Baughman, R.H.; Eckhardt, H.; Kertesz, M. Structure-property predictions for new planar forms of carbon: Layered phases containing sp^2 and sp atoms. *J. Chem. Phys.* **1987**, *87*, 6687–6699. [CrossRef]
33. Li, G.; Li, Y.; Liu, H.; Guo, Y.; Li, Y.; Zhu, D. Architecture of graphdiyne nanoscale films. *Chem. Commun.* **2010**, *46*, 3256–3258. [CrossRef]
34. Kang, B.; Lee, J.Y. Graphynes as Promising Cathode Material of Fuel Cell: Improvement of Oxygen Reduction Efficiency. *J. Phys. Chem. C* **2014**, *118*, 12035–12040. [CrossRef]
35. Kang, B.; Liu, H.; Lee, J.Y. Oxygen adsorption on single layer graphyne: A DFT study. *Phys. Chem. Chem. Phys.* **2014**, *16*, 974–980. [CrossRef] [PubMed]
36. Hwang, H.J.; Koo, J.; Park, M.; Park, N.; Kwon, Y.; Lee, H. Multilayer Graphynes for Lithium Ion Battery Anode. *J. Phys. Chem. C* **2013**, *117*, 6919–6923. [CrossRef]
37. Yang, Z.; Zhang, C.F.; Hou, Z.F.; Wang, X.; He, J.J.; Li, X.D.; Song, Y.W.; Wang, N.; Wang, K.; Wang, H.L.; et al. Porous hydrogen substituted graphyne for high capacity and ultra-stable sodium ion storage. *J. Mater. Chem. A* **2019**, *7*, 11186–11194. [CrossRef]
38. Wang, K.; Wang, N.; He, J.J.; Yang, Z.; Shen, X.Y.; Huang, C.S. Preparation of 3D Architecture Graphdiyne Nanosheets for High-Performance Sodium-Ion Batteries and Capacitors. *ACS Appl. Mater. Inter.* **2017**, *9*, 40604–40613. [CrossRef] [PubMed]
39. Yang, C.F.; Qiao, C.; Chen, Y.; Zhao, X.Q.; Wu, L.L.; Li, Y.; Jia, Y.; Wang, S.Y.; Cui, X.L. Nitrogen Doped gamma-Graphyne: A Novel Anode for High-Capacity Rechargeable Alkali-Ion Batteries. *Small* **2020**, *16*, 1907365. [CrossRef] [PubMed]

40. Xu, Z.; Lv, X.; Li, J.; Chen, J.; Liu, Q. A promising anode material for sodium-ion battery with high capacity and high diffusion ability: Graphyne and graphdiyne. *RSC Adv.* **2016**, *6*, 25594–25600. [CrossRef]
41. Ma, J.; Yuan, Y.; Wu, S.; Lee, J.Y.; Kang, B. γ-Graphyne nanotubes as promising lithium-ion battery anodes. *Appl. Surf. Sci.* **2020**, *531*, 147343. [CrossRef]
42. Zhou, W.; Shen, H.; Zeng, Y.; Yi, Y.; Zuo, Z.; Li, Y.; Li, Y. Controllable Synthesis of Graphdiyne Nanoribbons. *Angew. Chem. Int. Ed.* **2020**, *59*, 4908–4913. [CrossRef] [PubMed]
43. Li, G.; Li, Y.; Qian, X.; Liu, H.; Lin, H.; Chen, N.; Li, Y. Construction of Tubular Molecule Aggregations of Graphdiyne for Highly Efficient Field Emission. *J. Phys. Chem. C* **2011**, *115*, 2611–2615. [CrossRef]
44. Kresse, G.; Joubert, D. From ultrasoft pseudopotentials to the projector augmented-wave method. *Phys. Rev. B* **1999**, *59*, 1758–1775. [CrossRef]
45. Perdew, J.P.; Burke, K.; Ernzerhof, M. Generalized Gradient Approximation Made Simple. *Phys. Rev. Lett.* **1996**, *77*, 3865–3868. [CrossRef] [PubMed]
46. Monkhorst, H.J.; Pack, J.D. Special points for Brillouin-zone integrations. *Phys. Rev. B* **1976**, *13*, 5188–5192. [CrossRef]
47. Henkelman, G.; Uberuaga, B.P.; Jonsson, H. A climbing image nudged elastic band method for finding saddle points and minimum energy paths. *J. Chem. Phys.* **2000**, *113*, 9901–9904. [CrossRef]
48. Das, D.; Hardikar, R.P.; Han, S.S.; Lee, K.R.; Singh, A.K. Monolayer BC2: An ultrahigh capacity anode material for Li ion batteries. *Phys. Chem. Chem. Phys.* **2017**, *19*, 24230–24239. [CrossRef] [PubMed]